

Dissipative tunneling rates through the incorporation of first-principles electronic friction in instanton rate theory. II. Benchmarks and applications

Cite as: J. Chem. Phys. **156**, 194107 (2022); <https://doi.org/10.1063/5.0088400>

Submitted: 16 February 2022 • Accepted: 26 April 2022 • Accepted Manuscript Online: 26 April 2022 • Published Online: 17 May 2022

 Y. Litman,  E. S. Pócs,  C. L. Box, et al.



View Online



Export Citation



CrossMark

ARTICLES YOU MAY BE INTERESTED IN

[Dissipative tunneling rates through the incorporation of first-principles electronic friction in instanton rate theory. I. Theory](#)

The Journal of Chemical Physics **156**, 194106 (2022); <https://doi.org/10.1063/5.0088399>

[NQCDynamics.jl: A Julia package for nonadiabatic quantum classical molecular dynamics in the condensed phase](#)

The Journal of Chemical Physics **156**, 174801 (2022); <https://doi.org/10.1063/5.0089436>

[Nonadiabatic instanton rate theory beyond the golden-rule limit](#)

The Journal of Chemical Physics **156**, 174115 (2022); <https://doi.org/10.1063/5.0088518>

Lock-in Amplifiers
up to 600 MHz



Zurich
Instruments



Dissipative tunneling rates through the incorporation of first-principles electronic friction in instanton rate theory. II. Benchmarks and applications

Cite as: J. Chem. Phys. 156, 194107 (2022); doi: 10.1063/5.0088400

Submitted: 16 February 2022 • Accepted: 26 April 2022 •

Published Online: 17 May 2022



View Online



Export Citation



CrossMark

Y. Litman,^{1,a)} E. S. Pócs,¹ C. L. Box,² R. Martinazzo,³ R. J. Maurer,² and M. Rossi^{1,a)}

AFFILIATIONS

¹MPI for the Structure and Dynamics of Matter, Luruper Chaussee 149, 22761 Hamburg, Germany

²Department of Chemistry, University of Warwick, Coventry CV4 7AL, United Kingdom

³Department of Chemistry, Università degli Studi di Milano, Via Golgi 19, 20133 Milano, Italy

Note: This paper is part of the 2022 JCP Emerging Investigators Special Collection.

^{a)}Authors to whom correspondence should be addressed: yairlitman@gmail.com and mariana.rossi@mpsd.mpg.de

ABSTRACT

In Paper I [Litman *et al.*, J. Chem. Phys. (in press) (2022)], we presented the ring-polymer instanton with explicit friction (RPI-EF) method and showed how it can be connected to the *ab initio* electronic friction formalism. This framework allows for the calculation of tunneling reaction rates that incorporate the quantum nature of the nuclei and certain types of non-adiabatic effects (NAEs) present in metals. In this paper, we analyze the performance of RPI-EF on model potentials and apply it to realistic systems. For a 1D double-well model, we benchmark the method against numerically exact results obtained from multi-layer multi-configuration time-dependent Hartree calculations. We demonstrate that RPI-EF is accurate for medium and high friction strengths and less accurate for extremely low friction values. We also show quantitatively how the inclusion of NAEs lowers the crossover temperature into the deep tunneling regime, reduces the tunneling rates, and, in certain regimes, steers the quantum dynamics by modifying the tunneling pathways. As a showcase of the efficiency of this method, we present a study of hydrogen and deuterium hopping between neighboring interstitial sites in selected bulk metals. The results show that multidimensional vibrational coupling and nuclear quantum effects have a larger impact than NAEs on the tunneling rates of diffusion in metals. Together with Paper I [Litman *et al.*, J. Chem. Phys. (in press) (2022)], these results advance the calculations of dissipative tunneling rates from first principles.

© 2022 Author(s). All article content, except where otherwise noted, is licensed under a Creative Commons Attribution (CC BY) license (<http://creativecommons.org/licenses/by/4.0/>). <https://doi.org/10.1063/5.0088400>

I. INTRODUCTION

The transport kinetics of small molecules and atoms in metals play an important role in technological applications in several areas, such as fuel cells, batteries, and nuclear reactors, among others.^{1–4} In particular, accurate measurements of hydrogen diffusion are still experimentally challenging since the diffusion coefficients are very sensitive to the microstructure of the material and the composition of the alloy.^{5–7} As a consequence, reported values of diffusion

constants by different groups can be scattered over a few orders of magnitude.

First-principles calculations have the potential to provide an increased understanding of the transport dynamics of light particles in well-defined structures throughout a wide range of thermodynamic conditions (e.g., temperature and pressure), which can complement experiments and guide further developments. Most of the atomistic calculations performed to study nuclear dynamical processes rely on Newtonian dynamics on the ground-state adiabatic

potential energy surface (PES), as given by the Born–Oppenheimer approximation (BOA). However, the coupling of the nuclear movement with electrons in the metal can easily induce electronic excitations, which represent a breakdown of the BOA and give rise to non-adiabatic effects (NAEs).^{8,9} Furthermore, light particles, such as hydrogen and deuterium, can exhibit strong nuclear quantum effects (NQE), which can either increase or decrease its mobility through metals.^{10,11} As a consequence, an understanding of the interplay of NQEs and NAEs in the transport process of light atoms in realistic systems remains elusive.

Several exact methods to simulate non-adiabatic quantum dynamics have been developed in the last few decades.^{12–14} However, due to the unfavorable scaling of these theoretical approaches with the number of degrees of freedom, approximate but accurate and efficient methods are required to capture NQEs and NAEs in high-dimensional systems or to be used with costly *ab initio* potentials. In Paper I,⁶⁹ we presented the ring-polymer instanton with explicit friction (RPI-EF) theory for the calculation of dissipative thermal tunneling rates, which has the potential to fulfill these requirements. Briefly, RPI-EF allows for an easy and efficient incorporation of the electronic friction formalism, originally proposed by Helling and Persson¹⁵ and Head-Gordon and Tully,¹⁶ into the semi-classical ring-polymer instanton (RPI) rate theory.^{17–19} The imaginary-time propagation inherent to instanton theory results in a simple procedure for the determination of the instanton trajectory in RPI-EF, involving a saddle-point optimization on an effective potential modified by the friction tensor.

In this article, we show the merits and limitations of RPI-EF. We benchmark the accuracy of RPI-EF rate predictions by comparing them with numerically exact theories in model potentials. Subsequently, we examine the interplay of the reaction barrier height and friction strengths on the tunneling rate in 1D and 2D model potentials connected to a bath. Finally, the new approach is applied to hydrogen and deuterium hopping reactions in bulk transition metals, focusing on Pd, by employing Kohn–Sham density functional theory. These calculations allow for a quantitative analysis of the impact of different effects on the rate constants, such as the dimensionality of the system, NQEs, and NAEs.

This paper is structured as follows: In Sec. II, the methods employed to obtain the tunneling rates are briefly summarized and the simulation details for each one are specified. In Sec. III, the model potentials and the systems treated from first-principles are described. Results of numerical simulations on low-dimensional models for position-independent and position-dependent friction tensors are discussed in Secs. IV A and IV B, respectively. Finally, the first-principles results for the hydrogen and deuterium hopping in metals are discussed in Sec. V. Section VI concludes by summarizing the main results and giving an outlook to future directions.

II. RATE CALCULATION METHODS

A. Ring-polymer instanton (with explicit friction)

The RPI rate theory^{17,18} is a semi-classical method that allows for the calculation of tunneling rates. RPI theory can be interpreted as the extension of Eyring transition state theory (TST)²⁰ into the deep tunneling regime since the rates are evaluated utilizing only a limited amount (often a single) special configuration, circumventing

the necessity of real-time sampling. While in TST, this special configuration is the first-order saddle-point connecting reactants and products on the potential energy surface (PES), in RPI rate theory, the special configurations are found at the first-order saddle-points of the extended space of the ring polymer (RP) potential. These trajectories in imaginary time are known as instanton trajectories. The RPI rate expression is analogous to the one proposed by TST and reads

$$k_{\text{inst}}(\beta) \propto \lim_{P \rightarrow \infty} e^{-U_P^{\text{sys}}(\bar{q})/\hbar}, \quad (1)$$

where

$$U_P^{\text{sys}}(\mathbf{q}) = \sum_{k=1}^P \sum_{i=1}^{3N} m_i \frac{\omega_P^2}{2} (q_i^{(k)} - q_i^{(k+1)})^2 + \sum_{k=1}^P V(q_1^{(k)}, \dots, q_{3N}^{(k)}) \quad (2)$$

is the RP potential. In the previous equation, $q_i^{(k)}$ is the position of the i th degree of freedom of the k th bead of the ring polymer, m_i is the mass of the i th degree of freedom, N is the number of atoms, P is the number of beads (replicas), \mathbf{q} is an abbreviated notation to represent all the degrees of freedom, \bar{q} denotes the instanton geometry, and $\omega_P = (\beta_P \hbar)^{-1}$ with $\beta_P = \frac{1}{k_B P T}$.

In Paper I,⁶⁹ we showed how the RPI rate theory can be extended to compute tunneling rates for systems connected to a harmonic bath that simulates a dissipative environment. Irrespective of the dissipative mechanism and assuming that the environment degrees of freedom adjust adiabatically to the system position, one can fully characterize the system–environment coupling by a position (\mathbf{q}) and frequency (λ) dependent friction tensor, $\tilde{\eta}(\mathbf{q}, \lambda)$. Moreover, when the frequency and position dependence is decoupled, we proved that the RP potential that enters Eq. (1) is renormalized, adopting the form

$$U_P^{\text{eff}} = U_P^{\text{sys}} + \sum_{l=-P/2+1}^{P/2} \sum_{i=1}^{3N} \frac{\omega_l}{2} \left[\sum_{k=1}^P C_{lk} \left(\int_{q^{\text{ref}}}^{q^{(k)}} \tilde{\eta}(q', \omega_k)^{1/2} \cdot dq' \right) \right]^2, \quad (3)$$

where $\omega_l = 2\omega_P \sin(|l|\pi/P)$ are the free RP normal mode frequencies and \mathbf{C} is the transformation matrix between the RP normal modes and Cartesian coordinates. In the limiting case of a position-independent friction, the previous expression can be simplified to

$$U_P^{\text{eff}} = U_P^{\text{sys}} + \sum_{l=-P/2+1}^{P/2} \sum_{i=1}^{3N} \frac{\tilde{\eta}(\omega_l) \omega_l}{2} (Q_i^{(l)})^2, \quad (4)$$

where $Q^{(l)}$ represent the free RP normal mode coordinates.

The RPI calculations were performed using the i-PI²¹ code. The forces and energies required by the algorithm were passed to i-PI from an external code through an interface based on internet sockets. The RPI-EF calculations required an extension of the i-PI communication protocol. We added to the existing communication of the energy, forces, and stresses from external codes to i-PI, the possibility to pass additional information as JSON-formatted strings. In this way, it is possible to communicate any type of data, and more importantly, when the data are numeric, they become available to

be used by any implemented algorithm within i-PI. This enables the use of quantities beyond energies and forces that change along the simulation within different types of dynamics.

The FHI-aims code²² and an in-house Python code were used in connection to i-PI for the density-functional theory (DFT) and model calculations, respectively. Transition-state geometries were obtained either by the string method²³ combined with the climbing image technique²⁴ or using a minimum-mode-following algorithm,²⁵ as implemented in i-PI. The RPI calculations were initialized after finding the transition state by stretching the transition-state geometry along the mode with imaginary frequency using a number of replicas between 10 and 16. Optimizations were started at a temperature of 10 K below the corresponding crossover temperature, T_c° . After converging the instanton pathway for the first calculation, successive steps of temperature decrease and RP interpolation to increase the number of beads were performed until the target temperature was reached. If required, further calculations with more beads were performed to guarantee that in all cases and for all temperatures, the final rates were converged within a 10% error.^{26,27} See more details in Sec. I of the [supplementary material](#).

B. Multi-configuration time-dependent Hartree

Numerically exact results for selected models in this paper were obtained with the multi-layer variant^{28–30} of the multi-configuration time-dependent Hartree method^{31–32} (ML-MCTDH), as implemented in the Heidelberg package.³³ MCTDH is a variational method that relies on optimal, time-dependent basis functions to alleviate the exponential scaling problem of standard methods based on direct expansions on a time-independent basis. In the MCTDH ansatz, the wave function $|\Psi(t)\rangle$ is expanded on orthogonal configurations $|\Phi_J(t)\rangle$, which, in turn, are products of “single particle” functions (SPFs),

$$|\Psi(t)\rangle = \sum_J A_J(t) |\Phi_J(t)\rangle = \sum_J A_J(t) \prod_k |\phi_{j_k}^{(k)}\rangle(t), \quad (5)$$

and both the expansion coefficients (A_J) and the SPFs ($|\phi_{j_k}(t)\rangle$) are variationally optimized. Here, $J = (j_1, \dots, j_k, \dots, j_F)$ is a multi-index, the index $k = 1, 2, \dots, F$ runs over the single particles, and $j_k = 1, \dots, n_k$ labels the SPFs used for the k th mode. Conventional MCTDH uses single particles for each degree of freedom or small groups thereof and represents their SPFs by a direct expansion on a grid/basis-set (the so-called primitive grid) designed for the single particle at hand. This limits its capability of handling large systems. In contrast, in ML-MCTDH, the single particles are high-dimensional modes whose SPFs are described by further MCTDH expansions employing lower dimensional SPFs. The procedure can be indefinitely iterated until reasonably small single particles are defined that can be described on primitive grids. This recipe, similarly to tensor networks and matrix-product states,³⁴ endows the wave function with a hierarchical, flexible structure that allows for the treatment of considerably larger systems. In particular, ML-MCTDH has been successfully applied to the calculation of thermal rate constants in condensed-phase problems^{35,36} in the framework of the reactive flux-side approach, where $k(T)$ is given by the long-time limit of the equilibrium flux-side time-correlation function.^{37,38}

In this work, we followed closely the original work by Wang and Thoss,^{40,41} who introduced an importance sampling technique to recast the trace expression of the flux-side correlation function as an accessible ensemble-average over time-evolving wavepackets. In a nutshell, the evaluation of the rate constant is reduced to (i) a preparation step where the wavepackets are initialized by combining (system) Boltzmannized flux eigenvectors with bath states drawn from the canonical ensemble of the uncoupled bath, (ii) an equilibration step where imaginary-time dynamics introduces the correlations present in the coupled system, and (iii) a propagation step where the real-time dynamics is followed up to the onset of the kinetic regime (the long-time limit alluded to above). Details about the calculations, including an overview of the flux-side approach, the Monte Carlo sampling, the tree structure of the ML-MCTDH wave function, and the number of SPFs and the primitive grids used, are provided in Sec. II of the [supplementary material](#). Converged calculations were obtained with 50 bath modes and using 128–256 realizations for each value of T and coupling strength.

III. SIMULATION DETAILS AND PARAMETERS

A. 1D and 2D double-well models

We analyze the performance of RPI-EF on a double-well model similar to the ones usually employed to study quantum dynamics in system–bath models.^{39,40} The potential energy surface of the system is given by

$$V_{\text{DW}}(q) = -\frac{1}{2}m\omega^{\ddagger 2}(q - q_0)^2 + \frac{m^2\omega^{\ddagger 4}}{16V_0}q^4, \quad (6)$$

where, unless otherwise specified, we set m as the mass of atomic hydrogen and $\omega^{\ddagger} = 500 \text{ cm}^{-1}$. The coupling between the system and the bath can be made position-dependent according to⁴¹

$$f(q) = q[1 + \varepsilon_1 \exp(-\Delta q^2/2) + \varepsilon_2 \tanh(\Delta q)], \quad (7)$$

where $\Delta q = (q - q^{\ddagger})/\delta$, δ determines the length-scale of the nonlinear couplings, and ε_1 and ε_2 are the magnitudes of its symmetric and anti-symmetric components, respectively. The calculations with position-independent friction were obtained by setting $\varepsilon_1 = \varepsilon_2 = 0$. Naturally, the position-dependent couplings of real systems do not generally adopt such simple forms. However, as it will be shown in Sec. IV B, this simplified form will prove sufficient to expose the importance of including this position-dependence in the tunneling rates.

We consider an Ohmic (linear) spectral density multiplied by an exponential cutoff, leading to

$$\tilde{\eta}_{ii}(\mathbf{q}, \lambda) = \frac{2}{\pi} \int_0^{+\infty} d\omega \tilde{\eta}_0 \left(\frac{\partial f(\mathbf{q})_i}{\partial q_i} \right)^2 \frac{\lambda}{\omega^2 + \lambda^2} e^{-\omega/\omega_c}, \quad (8)$$

where $\tilde{\eta}_0$ is the static friction coefficient and, unless otherwise specified, we set $\omega_c = 500 \text{ cm}^{-1}$.

To illustrate the tensorial nature of the friction, we also considered a two-dimensional double double-well (DDW) potential given by

$$V_{\text{DDW}}(q_1, q_2) = V_{\text{DW}}(q_1) + V_{\text{DW}}(q_2) + Cq_1q_2, \quad (9)$$

where C is a constant to be specified. Additionally, for the sake of simplicity, we considered that the bath couples to each degree of freedom independently, and the coupling function is given by

$$f(q_1, q_2) = (f(q_1), f(q_2)), \quad (10)$$

where $f(q_i)$ is given by Eq. (7).

B. Fcc metals

We also perform first-principles atomistic simulations to showcase the methodology developed in this paper. More specifically, we focus on hydrogen and deuterium hopping reactions within interstitial sites in different bulk fcc metals: Pd, Pt, Cu, and Ag. The bulk systems were modeled by $2 \times 2 \times 2$ cubic supercells containing one hydrogen or deuterium atom and 32 metal atoms. Energies and forces were computed employing density-functional theory (DFT) using the FHI-aims²² code and the Perdew, Burke, and Ernzerhof (PBE) exchange–correlation functional.⁴² Geometries were relaxed using the standard *light* settings (in the case of Pd, increasing the radial multiplier to two) from FHI-aims until all forces were below 10^{-3} eV/Å. Minimum-energy pathways (MEPs) were obtained with the string method²³ combined with the climbing image technique²⁴ as implemented in the aimsChain package provided with the FHI-aims code. The BroydenBorn–FletcherBorn–GoldfarbBorn–Shanno (BFGS) algorithm was used as the optimization procedure, and the residual forces converged below 10^{-3} eV/Å. Unless specified otherwise, a $6 \times 6 \times 6$ k-point sampling was used. This setup ensures that errors in relative energies are below 1 meV/atom. We obtained lattice constants of 3.95, 3.97, 3.63, and 4.16 Å for Pd, Pt, Cu, and Ag, respectively, in good agreement with Ref. 43. See Sec. III A of the [supplementary material](#) for more details regarding convergence tests.

As explained in Paper I⁶⁹ of this paper, the electronic friction tensor was computed as

$$\tilde{\eta}_{ij}(\mathbf{q}, \lambda) = \hbar \sum_{v, v'} \langle \psi_v | \partial_i \psi_{v'} \rangle \langle \psi_{v'} | \partial_j \psi_v \rangle (f(\varepsilon_v) - f(\varepsilon_{v'})) \times \frac{\lambda \Omega_{vv'}}{\lambda^2 + \Omega_{vv'}^2}, \quad (11)$$

where $f(\varepsilon)$ is the state occupation given by the Fermi–Dirac distribution, ψ_v and ε_v are the KS electronic orbitals and orbital energies of the v th level, i and j label the nuclear degrees of freedom, $\partial_i = \partial/\partial q_i$, and $\Omega_{vv'} = (\varepsilon_v - \varepsilon_{v'})/\hbar$. The calculation of the non-adiabatic coupling elements was obtained through a finite-difference approach, as currently implemented in the FHI-aims code.⁴⁴ Equation (11) is the Laplace transform of the time-dependent electronic friction tensor, thus differing from expressions commonly used in the literature,⁴⁵ as we discussed in Paper I.⁶⁹ While the expression in Eq. (11) is the appropriate one for RPI-EF, other expressions have been correctly used for the calculation of vibrational lifetimes and molecular dynamics with electronic friction simulations in the Markovian limit.^{16,44,46,47} We used a step length of 0.001 Å for the finite-difference evaluation, and a $16 \times 16 \times 16$ k-point sampling for the friction tensor. We only calculated the tensor components related to the hydrogen or deuterium atoms. More details regarding convergence tests can be found in Sec. III B of the [supplementary material](#).

IV. NUMERICAL RESULTS ON MODEL POTENTIALS

A. Position-independent friction

We start by analyzing the linear coupling case and benchmarking the RPI-EF results against the ML-MCTDH results. In Fig. 1, the rate constants calculated for the DW potential [Eq. (6)] at different temperatures and friction values are shown. The RPI-EF results are in good agreement with the exact calculations for $\tilde{\eta}_0/m\omega^\ddagger > 0.1$ at all the temperatures considered. We note that the lowest temperature, 50 K, represents less than half of the crossover temperature evaluated without friction. Even at considerably higher friction values, where the RPI approach has been predicted to be inadequate,¹⁷ the agreement is quite remarkable, showing that real-time dynamical effects, such as recrossing, play a minor role in these cases. At lower friction values, specially below $\tilde{\eta}_0/m\omega^\ddagger = 0.05$, the agreement deteriorates. The poor performance of the RPI-EF method in the weak coupling regime is not surprising since the RPI predicts a finite value for the rate even at $\tilde{\eta}_0 = 0$, where the dynamics in such a 1D model would be described by a Rabi oscillation and, strictly speaking, a rate process cannot be defined. Indeed, RPI-EF reaches a plateau at $\tilde{\eta}_0/m\omega^\ddagger \approx 0.05$, which might be interpreted as “an intrinsic” dissipation inherent to that theory, as a consequence of ignoring recurrences that are associated with semiclassical pathways that leave the barrier region and make real-time bounces on the walls of the potential well. When η goes to zero, the exact results approach the limit of coherent tunneling dynamics, yielding ML-MCTDH rates that are larger than the ones calculated with RPI. In passing, we note that both methods present a minimum of the rate at around 70 K in the weak-friction regime (see the inset in Fig. 1), which differs from the low-temperature power law observed in metastable systems.^{48,49} A deeper study of this subtle but interesting quantum effect is beyond the scope of the current work and will be the subject of future research.

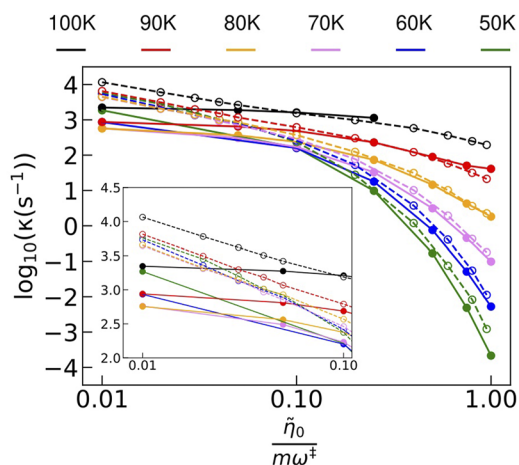


FIG. 1. Reaction rate constants for the DW potential ($V_0 = 258$ meV, $\omega_c = 500$ cm^{-1} , and $q_0 = 0$) for temperatures between 50 and 100 K for different friction values computed with RPI-EF (solid lines with filled circles) and ML-MCTDH (dashed lines with empty circles).

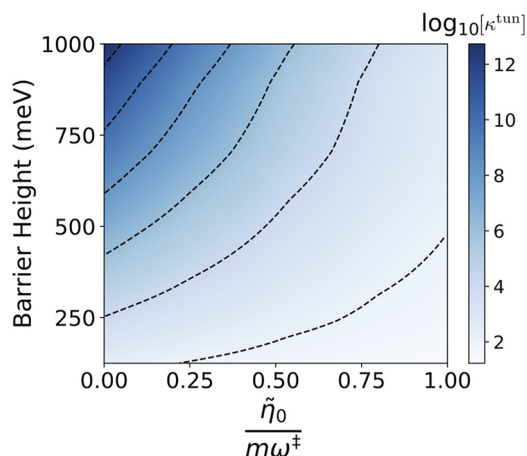


FIG. 2. Tunneling enhancement factors $\log_{10}[\kappa^{\text{tun}}]$ as a function of the energy barrier height and friction strength on the DW potential with $q_0 = 0.0 \text{ \AA}$ (symmetric reaction profile) at $T = 0.77T_c^\circ = 80 \text{ K}$. The color-scale is logarithmic, and contour lines are drawn for isosurfaces spaced by two logarithmic units.

One way to evaluate the relative importance of tunneling to the total rate is to analyze the tunneling enhancement factor, κ^{tun} , defined as

$$\kappa^{\text{tun}}(\beta, \tilde{\eta}) = \frac{k_{\text{inst}}(\beta, \tilde{\eta})}{k_{\text{TST}}(\beta, \tilde{\eta})}, \quad (12)$$

with $k_{\text{TST}}(\beta, \eta)$ being the TST rate.²⁶ Figures 2 and 3 show the calculated tunneling enhancement factors for different barrier heights and friction values for symmetric and asymmetric reactions, respectively. For the range of parameters considered here, it can be observed that the tunneling enhancement factor calculated with and without friction can differ up to almost ten orders of magnitude, that it increases with the increase in the barrier height, and that it decreases with the increasing friction strength. For barriers larger

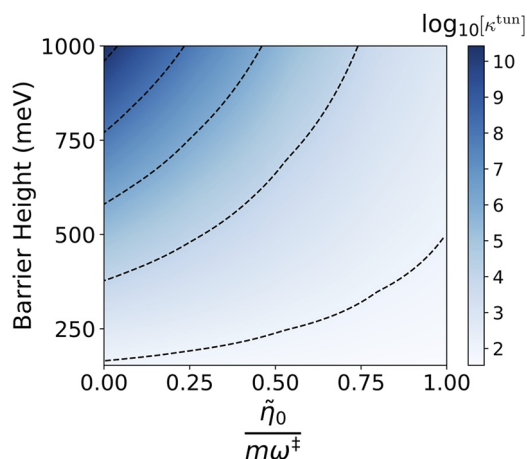


FIG. 3. Same as Fig. 2 with $q_0 = 0.08 \text{ \AA}$ (asymmetric reaction profile). The exoergic reaction is considered.

than 500 meV, the isosurfaces are approximately straight lines with a slope one, meaning that barrier heights and friction strengths have a comparable but opposite effect on tunneling.

We now proceed to discuss why the friction strength and the barrier height impact the tunneling contribution to the rate. The friction value determines the system–bath coupling strength. As evidenced by $\kappa^{\text{tun}} \sim 1$ at higher friction values, the stronger the coupling, the more classical the system behaves. However, the reason why the impact of the friction becomes more relevant at higher barrier heights is less straightforward to understand and requires the analysis of the instanton pathways. In Fig. 4, we show the decomposition of the instanton geometry into the free RP normal mode basis. We first consider the case without coupling to the bath. For symmetric barriers, Fig. 4(a), the instanton pathway expands only along the odd RP normal modes due to the symmetry of the underlying potential, and the first two degenerate RP normal modes ($l = \pm 1$) contribute with more than 99% to the path. For asymmetric barriers, Fig. 4(c), even though all normal modes are, in principle, allowed by symmetry, the first two degenerate RP normal modes exhibit the highest contribution with the centroid mode ($l = 0$) presenting a non-negligible contribution as well. For both barrier shapes, the population of the $l = \pm 1$ modes increases with the barrier height simply because the pathway from reactants to the product becomes longer. The same trends are observed for calculations with intermediate system–bath coupling, Figs. 4(c) and 4(d), where the only difference is an overall smaller population of the RP normal modes due to the shorter instanton pathway. Thus, higher barriers correlate with a relatively larger impact of the friction on the rate. This is due to an increase in the RP normal mode population, which leads to an increase in the last term in Eq. (4). We note that this might not be true for other barriers with arbitrary shapes.

Grote–Hynes (GH) theory^{50–52} defines a relationship between reaction rates obtained with a finite friction strength and those obtained with vanishing friction strength in the classical limit. In Paper I,⁶⁹ we showed an extension of GH theory to the deep tunneling regime for the case of position-independent friction. Briefly, we proposed that tunneling rates with finite friction strength—RPI-EF rates—at a given temperature can be related to tunneling rates without friction—RPI rates—performed at a scaled temperature. The scaling relation for the temperatures is given by

$$T_b/T_c^\circ = \sqrt{\left(\frac{\tilde{\eta}(\omega_l^b)}{2m\omega^\ddagger}\right)^2 \frac{1}{l^2} + \left(\frac{T_a}{T_c^\circ}\right)^2} - \frac{\tilde{\eta}(\omega_l^b)}{2m\omega^\ddagger} \frac{1}{l}, \quad (13)$$

where T_c° is the crossover temperature without friction, T_b is the target temperature at which the RPI-EF result is desired, T_a is the temperature at which the RPI calculation must be performed, and ω_l^b is the l free RP normal mode frequency at T_b . Since ω_l^b depends on T_b , this equation has to be solved self-consistently. Even though Eq. (13) must be fulfilled for all l , from Fig. 4, one can expect that considering only $\omega_{l=\pm 1}$ should be a good assumption.

In Fig. 5, the error obtained by computing the rate using only $\omega_{l=\pm 1}$ in Eq. (13) for different temperatures and coupling strengths in the symmetric DW potential is presented. The estimated RPI rates at the scaled temperatures are within one order of magnitude from the full RPI-EF rates for all friction strengths, but they are in better agreement for $\tilde{\eta}_0/m\omega^\ddagger < 0.5$. Similar accuracy is

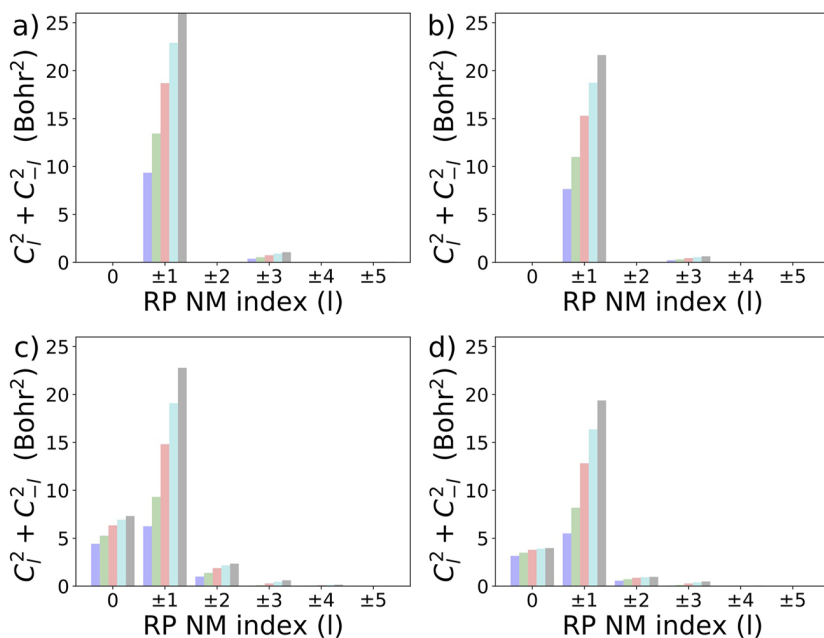


FIG. 4. Decomposition of instanton geometry into the free RP normal mode basis at a representative temperature of $T = 0.70T_c^\circ = 80$ K for (a) symmetric DW with $\tilde{\eta}_0/m\omega^\ddagger = 0.00$, (b) symmetric DW with $\tilde{\eta}_0/m\omega^\ddagger = 0.50$, (c) asymmetric DW ($q_0 = 0.08$ Å) with $\tilde{\eta}_0/m\omega^\ddagger = 0.00$, and (d) asymmetric DW ($q_0 = 0.08$ Å) with $\tilde{\eta}_0/m\omega^\ddagger = 0.50$. Five different barrier heights were considered: 125 meV (purple), 258 meV (green), 500 meV (red), 750 meV (light blue), and 1000 meV (gray). Coefficients are ordered and grouped by their corresponding RP normal mode (NM) index (l).

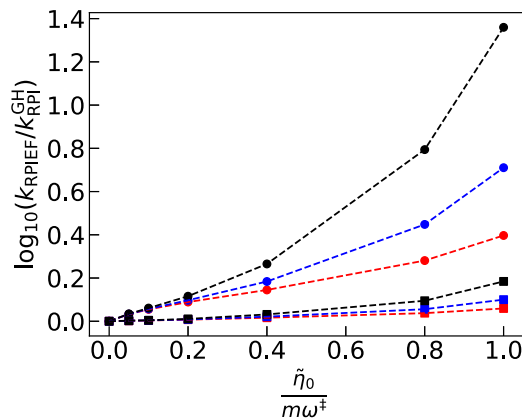


FIG. 5. Error on the RPI rate values obtained by the scaling relation shown in Eq. (13) ($k_{\text{RPI}}^{\text{GH}}$) compared to RPI-EF rates (k_{RPIEF}). The error is reported as the logarithm of the ratio between these rates in the symmetric DW model. Temperatures of $0.70T_c^\circ$ (squares) and $0.55T_c^\circ$ (circles) and reaction barriers of 258 meV (red), 500 meV (blue), and 1000 meV (black) are shown. An analogous plot for an asymmetric barrier is presented in the [supplementary material](#).

observed for an asymmetric DW model with this approximation even though the $l = 0$ mode is appreciably activated (see Sec. IV in the [supplementary material](#)).

B. Position-dependent friction

We now consider the case where the coupling between the system and the bath depends on the position of the system coordinate, i.e., a position-dependent friction. [Figure 6](#) shows instanton pathways obtained for different system–bath coupling strengths on a

DDW potential, as described by Eq. (9), at a temperature considerably lower than T_c° in this model. The parameters of the model were chosen such that the PES presents two global minima, two local minima, four first order saddle points that connect each global minimum with the closest local minimum, and one second order saddle point at $(q_1, q_2) = (0, 0)$, as shown in [Fig. 6\(a\)](#). The optimal tunneling pathway in the absence of dissipation is represented by the black curve in [Fig. 6](#), and it is a linear trajectory that connects the two global minima by crossing the second order saddle point. For $\tilde{\eta} > 0$, the anisotropy of the friction [see [Fig. 6\(b\)](#)] results in a modification of the instanton pathway, which bends toward regions of lower friction values. The magnitude of the bending of this path increases as the strength of the friction becomes larger. This shows that the optimal dissipative tunneling pathway is a compromise between the path with the shortest length, the path with the lowest potential energy, and the path with lowest friction. Indeed, for $\tilde{\eta}_0/m\omega^\ddagger > 0.5$, the dissipation is so strong close to the second-order saddle point that no instanton pathway that connects directly the two global minima can be found.

V. HOPPING OF HYDROGEN AND DEUTERIUM IN BULK METALS

A. Minimum energy paths, barrier heights, and friction strengths

Having characterized the performance of RPI-EF in model potentials, we now address the interplay of NAEs and NQEs on the hopping reaction of H within bulk metals, which we calculate from first-principles electronic-structure simulations.

We first analyze the MEP of the reactions in Pd, Pt, Cu, Ag, and Al. We note that we focus on the hopping reaction between neighboring octahedral \rightarrow tetrahedral interstitial sites. Even though

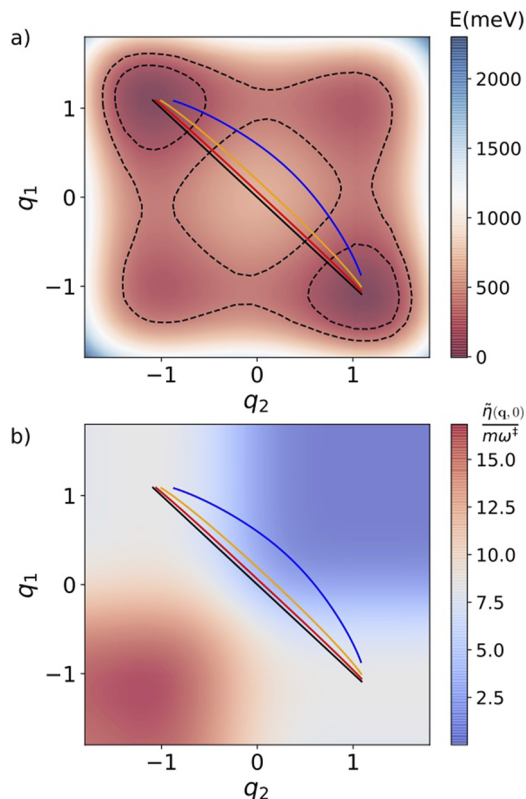


FIG. 6. Instanton pathways obtained at 40 K using the DDW model with $V_0 = 258$ meV, $q_0 = 0$ Å, $C = 97.1$ meV/Å² (0.001 a.u.), $\varepsilon_1 = 0$, $\varepsilon_2 = -0.8$, and $\Delta = 1.0$ for $\tilde{\eta}_0/m\omega^\ddagger = 0, 0.10, 0.25$, and 0.50 represented by full black, red, orange, and blue lines, respectively. The pathways are shown on top of (a) a heat map representing the underlying potential energy surface and (b) a heat map that helps visualize the position-dependence of the friction tensor. The map is computed as the sum of the diagonal elements of $\tilde{\eta}$ for $\tilde{\eta}_0/m\omega^\ddagger = 0.50$ [see Eqs. (8) and (10) in the main text].

in perfect solids these reactions determine the diffusion rate, in real materials other mechanisms might become the rate determining step of the diffusion process.^{53,54} A visualization of the MEP in Pd is shown in the inset of Fig. 7(b). In Table I, we report the reaction energy, reaction barrier, and electronic-friction values along the MEP for the reactions considered in this work. As shown in column 3, the energy barriers are in the 100–300 meV range in accordance with previous studies.⁵⁵

We continue by analyzing the electronic friction tensor $\tilde{\eta}_i(\mathbf{q}, \lambda)$ on the hydrogen atom along the MEPs. In Fig. 7(a), we present the electronic friction values evaluated at the first non-zero ring-polymer normal mode frequency at 100 K, projected onto the direction parallel to the reaction coordinate for the case of Pd. The friction values vary up to almost an order of magnitude, indicating the necessity of having a rate theory that takes into account such position dependence. The electronic friction along the MEP for the other metals shows a strong position dependence as well (see Sec. III B of the supplementary material). As shown in column 4 of Table I, the values vary from 0.7 to 3.1 ps⁻¹. The magnitude of the friction coefficients is large enough to impact vibrational lifetimes,⁴⁴

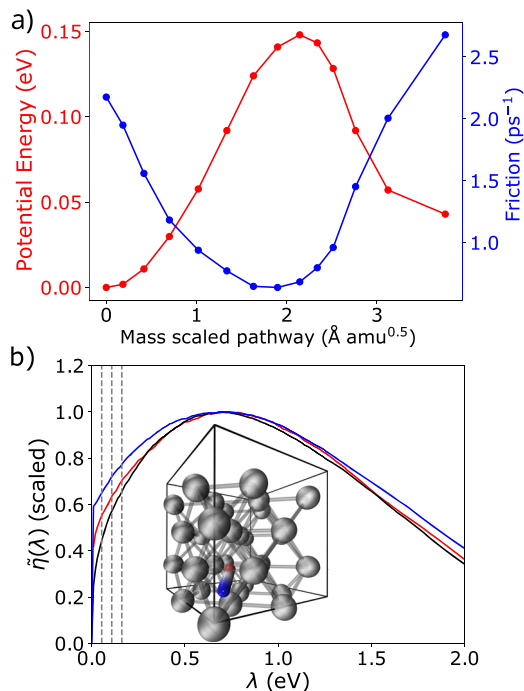


FIG. 7. (a) Minimum energy pathway (MEP) and friction along the reaction coordinate for the H hopping reaction in Pd (PBE functional). The energy is set to zero at the reactant geometry. (b) Frequency dependence of the friction tensor projected on the reaction coordinate at the reactant (red), transition state (black), and product (blue) states. To ease visual comparison, all curves in panel b have been scaled to adopt the value of one at the highest friction value. The first three non-zero ring-polymer normal mode frequencies at 100 K are depicted as vertical dashed gray lines. Inset: minimum energy pathway (MEP) corresponding to the hydrogen atom migrating from the octahedral site (red) to the tetrahedral site (blue). Pd atoms are depicted in gray.

adsorption mechanisms,⁵⁶ and scattering experiments.^{56,57} However, the dimensionless coefficient $\tilde{\eta}/m\omega^\ddagger$ yields at most a value of 0.05 (for Al), which, given the relatively low barrier heights, would result in a reduction in the tunneling rates by less than a factor of 5,

TABLE I. Reaction energy, $E_{T-O} = E_T - E_O$, and energy barrier heights, $E_{TS-O} = E_{TS} - E_O$, for the different fcc metals considered in this work. E_T , E_O , and E_{TS} refer to the potential energy corresponding to structures where the H atom is located at the tetrahedral (T), octahedral (O), and transition state (TS) sites, respectively. Values are reported without ZPE corrections. Minimum and maximum values adopted by the electronic friction, $\tilde{\eta}$, along the MEP are presented in column four. Values are evaluated at 54 meV (which corresponds to the first non-zero ring-polymer normal mode frequency at 100 K) and considering a projection of $\tilde{\eta}$ on the reaction coordinate. Columns 5 and 6 show the crossover temperature, T_c° , and imaginary frequency at the TS, ω^\ddagger , respectively.

System	E_{T-O} (meV)	E_{TS-O} (meV)	$\tilde{\eta}$ (ps ⁻¹)	T_c° (K)	ω^\ddagger (cm ⁻¹)
H@Pd	43	148	0.7–2.7	115	501
H@Pt	-35	44	0.8–2.8	96	420
H@Cu	188	300	0.7–1.1	140	612
H@Ag	52	160	0.7–1.0	116	504
H@Al	-71	88	1.8–3.1	84	365

according to our study on model potentials presented in Sec. IV A (see Figs. 2 and 3).

A closer look at the expression used to compute the electronic friction tensor, Eq. (11), allows us to rationalize the reasons behind such small coefficients.⁵⁸ Large friction values will arise in the case of a high DOS close to the Fermi level and due to the presence of hydrogen states close to the Fermi level. The former contributes to Eq. (11) via the Fermi–Dirac factors; the latter contributes via the strength of the nonadiabatic coupling. While the former depends mainly on the metal at hand, the latter is affected by both the impurity and the metal.⁵⁹ We analyzed the atomic projected DOS (see Sec. III C in the [supplementary material](#)) and confirmed that Pd and Pt are, at the same time, the systems that present the largest electronic friction values and the highest DOS at the Fermi level among the transition metals. Surprisingly, Al presents slightly larger friction values without a high DOS at the Fermi energy. This might suggest that the nonadiabatic couplings are comparatively large in this case. However, in all cases, the hydrogen atom neither creates new states nor affects the DOS appreciably in the vicinity of the Fermi level, which ultimately leads to rather small friction coefficients along the MEP for these systems.

Up to this point, we have considered values of the friction tensor at a single frequency. However, the calculation of the tunneling rates require the evaluation of the friction tensor at all the RP normal mode frequencies [Eq. (3)], and more importantly, in the derivation of RPI-EF with a position-dependent friction tensor, we have assumed that a separable coupling *ansatz* is valid. This *ansatz* is equivalent to assuming that the frequency dependence of the friction tensor remains the same at all (relevant) positions. As an illustrative example, we present in Fig. 7(b) the frequency dependence of the friction tensor at the stationary points of the MEP (reactant, transition, and product state) for the hydrogen hopping reaction in Pd. The frequency dependence shows a non-monotonic profile with a maximum around 0.6 eV and remains fairly similar along the MEP, suggesting that the non-adiabatic couplings in bulk metals are, to a great extent, well described by a “separable coupling.” This observation is equally valid for the other metals (see the [supplementary material](#), Sec. III B). A different type of coupling might be observed in scattering reactions, where atoms or molecules transition from vacuum to electron-rich environments.^{56,60} As discussed in Sec. IV A, only the first few ring-polymer normal modes are appreciably activated. For this reason, only a relatively small fraction of spectral density contributes to the rates [see Fig. 7(b)].

B. Tunneling rates: The case of Pd

We performed full-dimensional instanton calculations on Pd in order to gauge the predictive power of our studies on low-dimensional models and static estimators presented in Sec. IV. We selected Pd because it presents high values of friction along the MEP, and the diffusion of H in Pd has been well studied theoretically and experimentally before. In order to reduce the computational cost, we performed instanton calculations on a fcc cubic cell containing four Pd atoms and one H or D atom. These calculations were performed using a $12 \times 12 \times 12$ k-point sampling. The relatively small size of the unit cell induces an effective increase in the barrier when compared to larger unit cells, and the new T_c° increases to 136 K (see Sec. I in

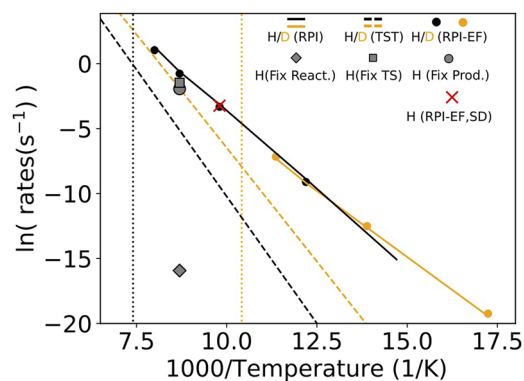


FIG. 8. Reaction rates for octahedral \rightarrow tetrahedral-site hopping reaction of H (black) and D (orange) in Pd, calculated by TST (dashed lines) and RPI rate theory (solid lines). RPI-EF rates with position-independent friction, fixed at a value of 4 ps^{-1} , are shown by black and orange circles for H and D, respectively, while the RPI-EF rates with position-dependent friction are depicted as a red cross. RPI rate calculations with the Pd atoms fixed at their reactant, transition, and product states are presented by diamond, square, and circle gray symbols, respectively. T_c° for H and D is marked by vertical black and orange dotted lines, respectively.

the [supplementary material](#)). Since the larger barriers magnify the effect of the friction on the rates, these calculations can be considered an upper-limit estimation of the impact of the friction on these rates.

In Fig. 8, the reaction rates for the hopping reaction of H and D in Pd from the octahedral to the tetrahedral site using TST, RPI theory, and RPI-EF theory are presented. At temperatures below T_c° , the tunneling effects, evidenced by the difference between the RPI and TST rates, become increasingly important, enhancing the rate by several orders of magnitude. The comparison of the TST predictions for H and D indicates an inverse kinetic isotope effect (KIE). The inverse KIE can be traced back to the softening of the normal modes orthogonal to the reaction pathway at the transition-state geometry.⁶¹ Since this effect is mainly due to ZPE, it is also present at temperatures above T_c and has been reported experimentally.⁵ Below T_c , the emergence of tunneling creates a competition between ZPE and tunneling effects as already reported by Kimizuka *et al.*⁶² Moreover, the similarity of the reaction rates for both isotopologues around 80 K is in agreement with the results of Ref. 62 and with experiments. However, the absolute values reported here are considerably smaller as a consequence of the rather small unit-cell employed in the calculations.

We now inspect the impact of the lattice on the reaction rates. For this purpose, we performed RPI calculations where the Pd atoms were fixed at the reactant, product, and transition state positions at 115 K. The rate obtained when the Pd atoms are fixed at their reactant positions is seven and four orders of magnitude slower than the RPI and TST estimates, respectively. This confirms the significant contribution of the lattice fluctuations to the reactive process¹⁰ and highlights the multidimensional nature of the reaction. In contrast, the rate estimates obtained from the calculations with the Pd atoms fixed at their transition-state or product positions are within an order of magnitude of the RPI estimates. The former result is expected since we are analyzing the rates at only 20 K below T_c° such

that the instanton pathway lies very close to the TS geometry. The latter result, instead, shows that the lattice relaxation between the transition state and the product is of comparatively lower relevance.

Finally, we consider the effect of the electronic friction on the rate. At 100 K, we performed a calculation with on-the-fly estimations of the friction tensor along the instanton pathway (also included in the instanton optimization). In order to gauge the importance of the spatial dependence of the friction, we also performed, at the same temperature, an instanton calculation using a constant value of 4 ps^{-1} for the friction (slightly higher than the maximum value reported in Table I). The results were numerically indistinguishable within the accuracy of our calculations, which may seem an unexpected result, at first. We proceeded to perform calculations with a constant and spatially independent friction value (which is less computationally demanding) at several other temperatures. In Fig. 8, we show these results, and as predicted by our earlier assessment, the friction coefficients are not large enough to produce a significant effect on the rates. This explains why the spatial dependence also does not appreciably change the rate constants.

VI. CONCLUSIONS

We have benchmarked the RPI-EF method and showed its performance in model potentials and first-principles calculations. By performing numerically exact simulations in 1D model systems including a spatially independent friction, we showed that RPI-EF yields accurate rates for all but very small friction coefficients at a much reduced computational cost. A systematic analysis of 1D and 2D double-well potentials allowed us to determine the magnitude of the decrease in the tunneling rates caused by friction as a function of the coupling strength and barrier height. We found that the suppression of tunneling is promoted by high coupling strengths and high energy barriers. We were also able to demonstrate that for a spatially dependent friction tensor, the instanton pathway can be considerably deformed toward low-friction regions when compared to the “non-dissipative” path (without friction). In comparison to previous similar approaches,^{63,64} the RPI-EF method is advantageous because it is highly efficient, more intuitive, and mathematically simpler.

In the context of reactions involving atoms and molecules in metallic environments, RPI-EF allows for the inclusion of NQEs and NAEs as described by an effective electronic friction. While here we used an electronic friction formulation that disregards electronic correlation,^{16,44,45} the RPI-EF approach is rather general and can be combined with other flavors of electronic friction that go beyond the independent quasi-particle picture. As a consequence of the relatively low computational cost of both RPI and the employed *ab initio* electronic friction formalism, RPI-EF allows the study of high-dimensional systems with on-the-fly *ab initio* evaluation of the forces and the electronic friction tensor.

In this work, we presented calculations of hydrogen and deuterium hopping between nearest interstitial sites of selected fcc metals, employing density-functional theory calculations. By evaluating the impact that different factors have on the reactions rates of this reaction in bulk Pd, we established that nuclear tunneling and lattice relaxation play a larger role in determining the magnitude of the rate than electronic friction. The latter turned out

to have a negligible impact on the reaction rates of these systems. This negative result, however, answers an important theoretical question regarding the interplay between NAEs (modeled by electronic friction) and NQEs⁶⁵ and also validates the rate constants currently used in this context for multiscale modeling.⁶⁶ Nonetheless, we anticipate that for impurities or adsorbates that present electronic levels in the vicinity of the Fermi energy of the metal, NAEs might play a more prominent role in connection with tunneling. We also expect to observe a larger effect for lighter particles, such as Muons,⁶⁷ or for surface reactions with higher energy barriers.⁶⁸

SUPPLEMENTARY MATERIAL

See the [supplementary material](#) for a detailed description of the MCTDH simulations and convergence tests of the DFT and RPI(-EF) calculations. Also included are rate estimations for the asymmetric double well potential and the DFT energies, electronic friction values, and the projected density of states along the MEP for the H hopping reaction in Pd, Pt, Ag, Cu, and Al.

ACKNOWLEDGMENTS

Y.L., E.S.P., and M.R. acknowledge financial support from the Max Planck Society and computer time from the Max Planck Computing and Data Facility (MPCDF). Y.L. and M.R. thank Jeremy Richardson, Aaron Kelly, and Stuart Althorpe for a critical reading of the manuscript. C.L.B. acknowledges financial support through an EPSRC-funded Ph.D. studentship. R.J.M. acknowledges Unimi for granting computer time at the CINECA HPC center. R.J.M. acknowledges financial support through a Leverhulme Trust Research Project Grant (No. RPG-2019-078) and the UKRI Future Leaders Fellowship program (Grant No. MR/S016023/1).

AUTHOR DECLARATIONS

Conflict of Interest

The authors have no conflicts to disclose.

DATA AVAILABILITY

The data that support the findings of this study are available from the corresponding author upon reasonable request.

REFERENCES

- ¹R. Mohtadi and S.-i. Orimo, *Nat. Rev. Mater.* **2**, 16091 (2016).
- ²I. M. Robertson, P. Sofronis, A. Nagao, M. L. Martin, S. Wang, D. W. Gross, and K. E. Nygren, *Metall. Mater. Trans. B* **46**, 1085 (2015).
- ³A. Traidia, E. Chatzidouros, and M. Jouiad, *Corros. Rev.* **36**, 323 (2018).
- ⁴L. Schlappbach and A. Züttel, *Nature* **414**, 353 (2001).
- ⁵J. Vökl and G. Alefeld, “Diffusion of hydrogen in metals,” in *Hydrogen in Metals I: Basic Properties*, edited by G. Alefeld and J. Vökl (Springer, Berlin, Heidelberg, 1978), pp. 321–348.
- ⁶S. Jothi, T. N. Croft, and S. G. R. Brown, *Int. J. Hydrogen Energy* **40**, 2882 (2015).
- ⁷Y. Fukai, *The Metal-Hydrogen System: Basic Bulk Properties* (Springer, Berlin, Heidelberg, 2005), pp. 303–400.

- ⁸H. Nienhaus, *Surf. Sci. Rep.* **45**, 1 (2002).
- ⁹A. M. Wodtke, *Chem. Soc. Rev.* **45**, 3641 (2016).
- ¹⁰H. Kimizuka, S. Ogata, and M. Shiga, *Phys. Rev. B* **97**, 014102 (2018).
- ¹¹H. Kimizuka and M. Shiga, *Phys. Rev. Mater.* **5**, 065406 (2021).
- ¹²M. H. Beck, A. Jäckle, G. A. Worth, and H.-D. Meyer, *Phys. Rep.* **324**, 1 (2000).
- ¹³Y. Tanimura and R. Kubo, *J. Phys. Soc. Jpn.* **58**, 101 (1989).
- ¹⁴G. Ilk and N. Makri, *J. Chem. Phys.* **101**, 6708 (1994).
- ¹⁵B. Hellsing and M. Persson, *Phys. Scr.* **29**, 360 (1984).
- ¹⁶M. Head-Gordon and J. C. Tully, *J. Chem. Phys.* **103**, 10137 (1995).
- ¹⁷J. O. Richardson and S. C. Althorpe, *J. Chem. Phys.* **131**, 214106 (2009).
- ¹⁸A. Arnaldsson, "Calculation of quantum mechanical rate constants directly from ab initio atomic forces," Ph.D. thesis, University of Washington, 2007.
- ¹⁹J. O. Richardson, *Int. Rev. Phys. Chem.* **37**, 171 (2018).
- ²⁰H. Eyring, *J. Chem. Phys.* **3**, 107 (1935).
- ²¹V. Kapil, M. Rossi, O. Marsalek, R. Petraglia, Y. Litman, T. Spura, B. Cheng, A. Cuzzocrea, R. H. Meißner, D. M. Wilkins, B. A. Helfrecht, P. Juda, S. P. Bienvenue, W. Fang, J. Kessler, I. Poltavsky, S. Vandenbrande, J. Wieme, C. Corminboeuf, T. D. Kühne, D. E. Manolopoulos, T. E. Markland, J. O. Richardson, A. Tkatchenko, G. A. Tribello, V. Van Speybroeck, and M. Ceriotti, *Comput. Phys. Commun.* **236**, 214 (2019).
- ²²V. Blum, R. Gehrke, F. Hanke, P. Havu, V. Havu, X. Ren, K. Reuter, and M. Scheffler, *Comput. Phys. Commun.* **180**, 2175 (2009).
- ²³W. E. W. Ren, and E. Vanden-Eijnden, *J. Chem. Phys.* **126**, 164103 (2007).
- ²⁴G. Henkelman, B. P. Uberuaga, and H. Jónsson, *J. Chem. Phys.* **113**, 9901 (2000).
- ²⁵J. Nichols, H. Taylor, P. Schmidt, and J. Simons, *J. Chem. Phys.* **92**, 340 (1990).
- ²⁶A. N. Beyer, J. O. Richardson, P. J. Knowles, J. Rommel, and S. C. Althorpe, *J. Phys. Chem. Lett.* **7**, 4374 (2016).
- ²⁷Y. Litman, "Tunneling and zero-point energy effects in multidimensional hydrogen transfer reactions: From gas phase to adsorption on metal surfaces," Ph.D. thesis, Freie Universität, Berlin, 2020.
- ²⁸H. Wang and M. Thoss, *J. Chem. Phys.* **119**, 1289 (2003).
- ²⁹U. Manthe, *J. Chem. Phys.* **130**, 054109 (2009).
- ³⁰O. Vendrell and H.-D. Meyer, *J. Chem. Phys.* **134**, 044135 (2011).
- ³¹H.-D. Meyer, U. Manthe, and L. S. Cederbaum, *Chem. Phys. Lett.* **165**, 73 (1990).
- ³²*Multidimensional Quantum Dynamics: MCTDH Theory and Applications*, edited by H.-D. Meyer, F. Gatti, and G. A. Worth (Wiley VCH, Weinheim, 2009).
- ³³G. A. Worth, M. H. Beck, A. Jäckle, O. Vendrell, and H.-D. Meyer, The MCTDH Package, Version 8.5, 2013, <http://mctdh.uni-hd.de/>.
- ³⁴J. I. Cirac, D. Pérez-García, N. Schuch, and F. Verstraete, *Rev. Mod. Phys.* **93**, 045003 (2021).
- ³⁵H. Wang, D. E. Skinner, and M. Thoss, *J. Chem. Phys.* **125**, 174502 (2006).
- ³⁶I. R. Craig, M. Thoss, and H. Wang, *J. Chem. Phys.* **127**, 144503 (2007).
- ³⁷W. H. Miller, S. D. Schwartz, and J. W. Tromp, *J. Chem. Phys.* **79**, 4889 (1983).
- ³⁸W. H. Miller, *J. Phys. Chem. A* **102**, 793 (1998).
- ³⁹M. Topaler and N. Makri, *J. Chem. Phys.* **101**, 7500 (1994).
- ⁴⁰I. R. Craig and D. E. Manolopoulos, *J. Chem. Phys.* **122**, 084106 (2005).
- ⁴¹J. B. Straus, J. M. Gomez Llorente, and G. A. Voth, *J. Chem. Phys.* **98**, 4082 (1993).
- ⁴²J. P. Perdew, K. Burke, and M. Ernzerhof, *Phys. Rev. Lett.* **77**, 3865 (1996).
- ⁴³P. Haas, F. Tran, and P. Blaha, *Phys. Rev. B* **79**, 085104 (2009).
- ⁴⁴R. J. Maurer, M. Askerka, V. S. Batista, and J. C. Tully, *Phys. Rev. B* **94**, 115432 (2016).
- ⁴⁵W. Dou, G. Miao, and J. E. Subotnik, *Phys. Rev. Lett.* **119**, 046001 (2017).
- ⁴⁶A. C. Luntz and M. Persson, *J. Chem. Phys.* **123**, 074704 (2005).
- ⁴⁷S. Monturet and P. Saalfrank, *Phys. Rev. B* **82**, 075404 (2010).
- ⁴⁸H. Grabert, U. Weiss, and P. Hanggi, *Phys. Rev. Lett.* **52**, 2193 (1984).
- ⁴⁹H. Grabert, P. Olschowski, and U. Weiss, *Phys. Rev. B* **36**, 1931 (1987).
- ⁵⁰R. F. Grote and J. T. Hynes, *J. Chem. Phys.* **73**, 2715 (1980).
- ⁵¹R. F. Grote and J. T. Hynes, *J. Chem. Phys.* **74**, 4465 (1981).
- ⁵²E. Pollak, *J. Chem. Phys.* **85**, 865 (1986).
- ⁵³D. Di Stefano, M. Mrovec, and C. Elsässer, *Acta Mater.* **98**, 306 (2015).
- ⁵⁴A. Pedersen and H. Jónsson, *Acta Mater.* **57**, 4036 (2009).
- ⁵⁵P. Ferrin, S. Kandoi, A. U. Nilekar, and M. Mavrikakis, *Surf. Sci.* **606**, 679 (2012).
- ⁵⁶O. Bünermann, H. Jiang, Y. Dorenkamp, A. Kandratsenka, S. M. Janke, D. J. Auerbach, and A. M. Wodtke, *Science* **350**, 1346 (2015).
- ⁵⁷A. Kandratsenka, H. Jiang, Y. Dorenkamp, S. M. Janke, M. Kammiller, A. M. Wodtke, and O. Bünermann, *Proc. Natl. Acad. Sci. U. S. A.* **115**, 680 (2018).
- ⁵⁸M. Forsblom and M. Persson, *J. Chem. Phys.* **127**, 154303 (2007).
- ⁵⁹L. Lecroart, N. Hertl, Y. Dorenkamp, H. Jiang, T. N. Kitsopoulos, A. Kandratsenka, O. Bünermann, and A. M. Wodtke, *J. Chem. Phys.* **155**, 034702 (2021).
- ⁶⁰R. J. Maurer, B. Jiang, H. Guo, and J. C. Tully, *Phys. Rev. Lett.* **118**, 256001 (2017).
- ⁶¹J. Meisner and J. Kästner, *Angew. Chem., Int. Ed.* **55**, 5400 (2016).
- ⁶²H. Kimizuka, S. Ogata, and M. Shiga, *Phys. Rev. B* **100**, 024104 (2019).
- ⁶³A. O. Caldeira and A. J. Leggett, *Ann. Phys.* **149**, 374 (1983).
- ⁶⁴U. Weiss, *Quantum Dissipative Systems*, 3rd ed. (World Scientific, 2008).
- ⁶⁵W. Dou and J. E. Subotnik, *J. Chem. Phys.* **148**, 230901 (2018).
- ⁶⁶C. Hüter, P. Shanthraj, E. McEniry, R. Spatschek, T. Hickel, A. Tehranchi, X. Guo, and F. Roters, *Metals* **8**, 430 (2018).
- ⁶⁷H. Teichler, *Phys. Lett. A* **64**, 78 (1977).
- ⁶⁸E. d. V. Gómez, S. Amaya-Roncancio, L. B. Avalle, D. H. Linares, and M. C. Gimenez, *Appl. Surf. Sci.* **420**, 1 (2017).
- ⁶⁹Y. Litman, E. S. Pócs, C. L. Box, R. Martinazzo, R. J. Maurer, and M. Rossi, *J. Chem. Phys.* (in press) (2022).